Available online at www.sciencedirect.com

ScienceDirect

Underground Space 9 (2023) 1–19

www.keaipublishing.com/undsp

Study on the long-term performance of shield tunnel passing through the gas-bearing strata

Jie He [a,b], Xiangyang Wei [a,c], Mei Yin [a,b,d,*]

[a] College of Civil Engineering, Tongji University, Shanghai 200092, China
[b] State Key Laboratory for Disaster Reduction in Civil Engineering, Tongji University, Shanghai 200092, China
[c] Key Laboratory of Geotechnical and Underground Engineering of Ministry of Education, Tongji University, Shanghai 200092, China
[d] Civil and Environmental Engineering Department, Brunel University London, London UB8 3PH, UK

Received 11 May 2022; received in revised form 15 July 2022; accepted 21 August 2022
Available online 27 September 2022

Abstract

When the shield tunnel passes through the gas-bearing strata, gas and water leakage may occur depending on the sealing performance of the segment joints. This process involves the complex multiphase seepage flow phenomenon in unsaturated soil. In this study, a fully coupled solid-liquid-gas model of the GIL Utility Tunnel was established to investigate the influence of the high-pressure gas on the mechanical properties of the tunnel segments and joints. The constitutive model of the Extended Barcelona Basic Model was implemented to simulate the effect of the seepage process on soil deformation. The results show that significant upward displacement occurred in the gas reservoir and its overlying strata, and the maximum displacement reached 30 mm. In addition, during the leakage of the gas and the water, an increase in the average soil effective stress was observed. It would induce a reduction in the suction and expansion of the yield surface. The tunnel tended to be stable from 20 years onwards, thus the soil deformation due to the water leakage only occurred at the early stage. In addition, the joint opening under the most unfavorable internal force combination was 0.69 mm, and the corresponding bolt stress was 119.5 MPa, which is below the yield limit. The results of this study help to understand the influence of high-pressure gas on tunnel safety and the sealing performance of the joints.

Keywords: A coupled solid-liquid-gas model; Unsaturated soil; Multiphase seepage; Gas-bearing strata; Shield tunnel; FEM

1 Introduction

Natural gas widely exists in the Yangtze River Delta of China. The existence of the gas-bearing strata poses a certain threat to the construction of underground infrastructures (Ding et al., 2017; Gong et al., 2018; Zhu et al., 2022). An engineering accident in the Hangzhou Metro Line 1 project in China reported by Guo et al. (2010), was induced by the high-pressure natural gas underneath the tunnel. In addition, the threat of the shallow gas-bearing strata was also found during the construction of the Chongming Cross-River Tunnel in Shanghai (Guo et al., 2013, Zhu et al., 2022). During the tunneling in gas-bearing strata, some explosion accidents happened after the gas gushed into the tunnel and reached the explosion limit (e.g., Wuluo Road No. 1 Tunnel, Sichuan; Qishanyan Tunnel, Guizhou; Tunnel of Yangjiahe Hydropower Station, Shaanxi; and Zhaxi Tunnel, Yunnan). In the recent project of Sutong GIL Utility Tunnel, the geological investigation report revealed the potential risks due to the shallow gas-bearing strata, where the high-pressure gas and water may leak through the segmental joints. Therefore, it is necessary to investigate the influence of the high-pressure gas on the mechanical properties of the tunnel segments and joints prior to the construction.

* Corresponding author at: Civil and Environmental Engineering Department, Brunel University, London, UK.
E-mail address: mei.yin@brunel.ac.uk (M. Yin).

https://doi.org/10.1016/j.undsp.2022.08.001

A series of research has been carried out on the modeling of the shallow gas-bearing strata. However, the mechanism of the migration of the gases as well as its effects on the coupled solid-liquid-gas properties of the underground infrastructures is still not clear. The migration process of the gas in the gas-bearing strata involves the complex multiphase seepage flow, which can be considered a multiphysics coupling problem in unsaturated soils (Yang, 1992). Biot (1941) firstly established a fully coupled hydro-mechanical model to simulate the consolidation of the saturated soil. As for the unsaturated soil, Bishop (1959) established the effective stress model of the unsaturated soil, considering the gas and water pressures in the soil. Alonso et al. (1990) and Pedroso and Farias (2011) introduced effective stress and suction as two independent stress variables into the constitutive model of the unsaturated soil, which is able to simulate the soil collapse behavior due to wetting. On the other hand, a series of numerical analyses have been performed on the multiphase seepage flow. Yang (1992) developed a two-dimensional generalized consolidation nonlinear numerical model of the unsaturated soil. Based on Fredlund's unsaturated soil theory, Liao and Jian (2008) conducted a numerical study on the multiphase seepage flow and the surface settlement due to the precipitation in deep foundation pit excavation. Cai et al. (2013) simulated the thermo-hydro-mechanical coupling process of high-level radioactive waste disposal based on the finite element method. Nagel and Meschke (2010) established a three-phase fully coupled finite element model considering the interaction between the soil skeleton, the pore water, and the air of the partially saturated soil. This model was used to simulate the compressed air support in tunneling. Wang et al. (2018) proposed a numerical model for the gas-bearing ground and applied it to the analysis of the ground deformation due to the controlled gas release in Hangzhou Bay of China. It was shown that the main deformation of the reservoir sand was caused by the increase of net mean stress induced by the reduction of the gas pressure in the reservoir. Qi et al. (2018) developed a solid-liquid-gas coupling model to simulate the harmful gas eruption in shield tunneling. Using this model, the harmful gas eruptions in the shield construction could be predicted. Feng et al. (2021) established a solid-liquid-gas coupling model to study the influences of the gas on the tunnel segment and the adjacent soils due to the gas leakage under the assumption that the shape of the gas pocket was simplified as a sphere in the numerical model.

Although several numerical studies have been carried out on the fully coupled solid-liquid-gas behavior of the unsaturated soil, studies on the effects of the high-pressure gas on the mechanical properties of the tunnel segments and joints are rarely reported. In this paper, a fully coupled solid-liquid-gas model is established to investigate the migrations of the high-pressure gas and water, as well as their influences on the mechanical properties of the tunnel linings. Different from the gas storage mode of pocket, the biogas occurrence state is assumed as a "gas reservoir" mode in this study. The results have also been used to evaluate the safety of the tunnels and the sealing behavior of the segment joints.

2 Fully coupled solid-liquid-gas model

2.1 Mass and momentum conservation equations

The unsaturated soil comprises the solid phase (s), the liquid phase (w), and the gas phase (g), which can be equivalent to the three-phase continuous medium. The continuity equations can be established based on the principle of mass conservation (Hu, 2013). For each phase ξ ($\xi = \mathrm{s}, \mathrm{w}, \mathrm{g}$), define the volume fraction n_ξ and the intrinsic density ρ_ξ as

$$n_\xi = \frac{\mathrm{d}v^\xi}{\mathrm{d}v}, \tag{1a}$$

$$\rho_\xi = \frac{\mathrm{d}m^\xi}{\mathrm{d}v^\xi}, \tag{1b}$$

where $\mathrm{d}v^\xi$ is the volume of the phase ξ, $\mathrm{d}v$ is the total volume, and $\mathrm{d}m^\xi$ is the mass of the phase ξ. Define the saturation as $S = n_\mathrm{w}/(n_\mathrm{w} + n_\mathrm{g})$, the porosity as $\phi = n_\mathrm{w} + n_\mathrm{g}$, and the void ratio as $e = (n_\mathrm{w} + n_\mathrm{g})/n_\mathrm{s}$.

According to the principle of mass conservation,

$$\frac{\mathrm{d}^\xi}{\mathrm{d}t}(\rho_\xi n_\xi) + \rho_\xi n_\xi \nabla \cdot \boldsymbol{v}^\xi = 0, \tag{2}$$

where $\boldsymbol{v}^\xi$ is the velocity of the phase ξ.

For the solid phase, $\xi = \mathrm{s}$, $n_\mathrm{s} = 1 - \phi$, and $\rho_\mathrm{s} =$ constant, and Eq. (2) can be written as

$$\frac{\mathrm{d}^\mathrm{s}\phi}{\mathrm{d}t} - (1-\phi)\nabla \cdot \boldsymbol{v}^\mathrm{s} = 0. \tag{3}$$

As for the liquid phase, $\xi = \mathrm{w}$, $n_\mathrm{w} = \phi S$, and $\rho_\mathrm{w} =$ constant, thus

$$\frac{\mathrm{d}^\mathrm{w}}{\mathrm{d}t}(\rho_\mathrm{w}\phi S) + \rho_\mathrm{w}\phi S \, \nabla \cdot \boldsymbol{v}^\mathrm{w} = 0. \tag{4}$$

Take the solid phase as the reference configuration, then

$$\frac{\mathrm{d}^\mathrm{s}}{\mathrm{d}t}(\rho_\mathrm{w}\phi S) + \nabla \cdot (\rho_\mathrm{w}\phi S \, \boldsymbol{v}^\mathrm{ws}) + \rho_\mathrm{w}\phi S \, \nabla \cdot \boldsymbol{v}^\mathrm{s} = 0 \tag{5}$$

where $\boldsymbol{v}^\mathrm{ws} = \boldsymbol{v}^\mathrm{w} - \boldsymbol{v}^\mathrm{s}$ is the velocity of the liquid phase relative to the solid phase. Define the Darcy velocity as $\tilde{\boldsymbol{v}}^\mathrm{ws} = \phi S \boldsymbol{v}^\mathrm{ws}$ and introduce the generalized Darcy's law:

$$\tilde{\boldsymbol{v}}^\mathrm{ws} = -\frac{\boldsymbol{\kappa} k_\mathrm{rw}}{\mu_\mathrm{w}}(\nabla p_\mathrm{w} - \rho_\mathrm{w}\boldsymbol{g}), \tag{6}$$

where $\boldsymbol{\kappa}$ is the soil intrinsic permeability tensor, k_rw is the relative permeability of the water phase, μ_w is the water phase dynamic viscosity, p_w is the water pressure, and $\boldsymbol{g}$ is the gravity acceleration.

By substituting Eqs. (3) and (6) into Eq. (5), it yields the following equation:

$$\phi\frac{\mathrm{d}^{\mathrm{s}}S}{\mathrm{d}t}+\nabla\cdot\left(-\frac{\boldsymbol{\kappa}k_{\mathrm{rw}}}{\mu_{\mathrm{w}}}(\nabla p_{\mathrm{w}}-\rho_{\mathrm{w}}\boldsymbol{g})\right)+S\nabla\cdot\boldsymbol{v}^{\mathrm{s}}=0. \tag{7}$$

Define the water phase residual saturation as $S_{\mathrm{s}}=n_{\mathrm{ws}}/(n_{\mathrm{w}}+n_{\mathrm{g}})$, where n_{ws} is the residual volume fraction of the water phase. The effective saturation of the water phase S_{e} is defined as:

$$S_{\mathrm{e}}=(S-S_{\mathrm{s}})/(1-S_{\mathrm{s}}), \tag{8}$$

which has a functional relationship with the matrix suction s, i.e.,

$$S_{\mathrm{e}}=S_{\mathrm{e}}(s), \tag{9}$$

where $s=p_{\mathrm{g}}-p_{\mathrm{w}}$ is the matrix suction, and p_{g} is the gas pressure. This relationship refers to the soil–water characteristic curve. The Van Genuchten Model (Van Genuchten, 1980) was used to define this soil–water characteristic curve:

$$S_{\mathrm{e}}=\left(\frac{1}{1+(\alpha s)^{n}}\right)^{m}. \tag{10}$$

Considering the effect of the residual saturation S_{s} and substituting Eq. (10) into Eq. (8), the saturation S can be expressed as follows:

$$S=\left(\frac{1}{1+(\alpha s)^{n}}\right)^{m}(1-S_{\mathrm{s}})+S_{\mathrm{s}}, \tag{11}$$

where α, m, and n are the material constants.

Therefore,

$$S(s)=S_{\mathrm{e}}(1-S_{\mathrm{s}})+S_{\mathrm{s}}. \tag{12}$$

Substituting Eq. (12) into Eq. (7), the continuity equation for the liquid phase can be written as

$$-\phi\frac{\partial S}{\partial s}\frac{\partial p_{\mathrm{w}}}{\partial t}+\phi\frac{\partial S}{\partial s}\frac{\partial p_{\mathrm{g}}}{\partial t}+\nabla\cdot\left(-\frac{\boldsymbol{\kappa}k_{\mathrm{rw}}}{\mu_{\mathrm{w}}}(\nabla p_{\mathrm{w}}-\rho_{\mathrm{w}}\boldsymbol{g})\right)+S\frac{\partial\varepsilon_{\mathrm{v}}}{\partial t}=0. \tag{13}$$

For the gas phase, the continuity equation is as follows:

$$\left(\frac{\phi(1-S)}{p_{\mathrm{g}}}-\phi\frac{\partial S}{\partial s}\right)\frac{\partial p_{\mathrm{g}}}{\partial t}+\phi\frac{\partial S}{\partial s}\frac{\partial p_{\mathrm{w}}}{\partial t}+\nabla\cdot\left(-\frac{\boldsymbol{\kappa}k_{\mathrm{rg}}}{\mu_{\mathrm{g}}}(\nabla p_{\mathrm{g}}-\rho_{\mathrm{g}}\boldsymbol{g})\right)+(1-S)\frac{\partial\varepsilon_{\mathrm{v}}}{\partial t}=0, \tag{14}$$

where k_{rg} is the relative permeability of the gas phase, and μ_{g} is the dynamic viscosity of the gas.

For the momentum conservation equation, the quasi-static process was considered:

$$\nabla\cdot(\dot{\boldsymbol{\sigma}}'+\dot{p}_f\boldsymbol{\delta})-\dot{\rho}\boldsymbol{g}=0, \tag{15}$$

where $\boldsymbol{\sigma}'$ is the effective stress, ρ is the soil density, $\rho=\rho_0+S(\rho_{\mathrm{sat}}-\rho_0)$, ρ_0 signifies the soil dry density, and ρ_{sat} is the soil saturated density. Define the effective stress as $\boldsymbol{\sigma}'=\boldsymbol{\sigma}_{\mathrm{tot}}-p_{\mathrm{f}}\boldsymbol{\delta}$, in which $p_{\mathrm{f}}=(Sp_{\mathrm{w}}+(1-S)p_{\mathrm{g}})$ is the equivalent fluid pressure, and $\boldsymbol{\delta}$ is the Kronecker Delta tensor.

In order to verify the fully coupled solid-liquid-gas model as discussed above, a finite element model was developed to simulate the "Liakopoulos drainage test" (Liakopoulos, 1964). The results are discussed in the Appendix.

2.2 Constitutive model for the unsaturated soil

In this study, the Barcelona Basic Model (BBM) (Alonso et al., 1990) and the Extended Barcelona Basic Model (BBMx) (Pedroso & Farias, 2011) were introduced to describe the elastoplastic behavior of the unsaturated soil.

(1) Elastic behavior

$$\dot{\varepsilon}_{\mathrm{v}}^{\mathrm{e}}=\frac{1}{K}\dot{p}+\frac{1}{K_{\mathrm{c}}}\dot{s}, \tag{16}$$

$$\dot{\varepsilon}_{\mathrm{s}}^{\mathrm{e}}=\frac{\dot{q}}{3G}, \tag{17}$$

where $\varepsilon_{\mathrm{v}}^{\mathrm{e}}$ is the elastic volumetric strain, and $\varepsilon_{\mathrm{s}}^{\mathrm{e}}$ is the elastic shear strain; $K=\frac{(1+e)p}{\kappa}$, $K_{\mathrm{c}}=\frac{(1+e)s}{\kappa_{\mathrm{s}}}$, and $G=\frac{2K(1-2\mu)}{3(1+\mu)}$, in which κ and κ_{s} are the rebound coefficients corresponding to the average stress and the suction, respectively, μ is the Poisson's ratio, and $e=(1+e_0)\varepsilon_{\mathrm{v}}+e_0$ is the void ratio, where e_0 is the initial void ratio, and ε_{v} is the volumetric strain.

(2) Effect of the suction on the compressibility

The suction affects the compressibility of the soil. It has been found that the higher the suction, the lower the compressibility. The relationship between the compression coefficient and the suction is shown as

$$\lambda(s)=\lambda_0\left[(1-r)\exp\left(-\frac{s}{\beta}\right)+r\right], \tag{18}$$

where λ_0 is the initial compression coefficient; r and β are the fitting parameters.

(3) Influence of the suction on the soil's tensile strength

The behavior of the suction contributes to the soil's tensile strength, which also affects the yield surface. It is considered as the linear relationship as below:

$$p_{\mathrm{s}}=k_{\mathrm{c}}s, \tag{19}$$

where p_{s} is the tensile strength of the soil, and k_{c} is the proportional coefficient.

(4) Influence of the suction on the pre-consolidation pressure

Due to the unsaturated state, the pre-consolidation pressure of the soil is affected by the suction as follows:

$$p_0(z_0, s) = p_{\text{ref}} \left(\frac{z_0}{p_{\text{ref}}} \right)^{\psi(s)}, \tag{20}$$

$$\psi(s) = \frac{\lambda_0 - \kappa}{\lambda(s) - \kappa}, \tag{21}$$

where λ, λ_0, and κ are the parameters defined above, p_{ref} is the reference stress, and z_0 is the intercept of the yield surface on the p-axis, which is used as the strengthening parameter to characterize the yield surface position. Equation (20) is the loading-collapse curve equation (LC curve).

(5) Yield surface equation

Taking the modified Cam-Clay model as the basic framework and combining the Matsuoka-Nakai criterion (Matsuoka & Nakai, 1974) to consider the strength reduction of the soil during extension, the yield surface of the BBMx model is.

$$F(p, q, \theta, z_0, z_1, s) = q^2 - M(\theta)^2 (p + p_s)(p_0 - p) + C \tag{22}$$

with

$$M(\theta) = M_{\text{cs}} \left(\frac{2\omega}{1 + \omega - (1 - \omega)\sin 3\theta} \right)^{\frac{1}{4}}, \tag{23}$$

$$\theta = \frac{1}{3} \arcsin \left(\frac{9\sqrt{2}\det(\boldsymbol{\sigma}' - p\boldsymbol{\delta})}{\sqrt{3} \| \boldsymbol{\sigma}' - p\boldsymbol{\delta} \|^3} \right), \tag{24}$$

$$\omega = \left(\frac{3 - \sin\phi}{3 + \sin\phi} \right)^4, \tag{25}$$

$$M_{\text{cs}} = \frac{6\sin\phi}{3 - \sin\phi}, \tag{26}$$

$$C(z_1, s) = p_{\text{ref}}^2 \left\{ \exp\left[\frac{(s - z_1)B}{p_{\text{ref}}} \right] - \exp\left(\frac{-z_1 B}{p_{\text{ref}}} \right) \right\}, \tag{27}$$

where $M(\theta)$ is the slope of the critical state line for the modified Cam-Clay model on the $q - p$ plane; $C(z_1, s)$ is introduced to form a smooth transition between the yield surfaces; B is the dimensionless parameter that controls the smoothness; z_1 is the maximum suction that the soil has been subjected to, and it also serves as the strengthening parameter to characterize the yield surface position.

3 Finite element modeling of the GIL utility tunnel

3.1 Model geometry

In order to simulate the multiphase seepage flow and its influence on the behaviors of the soil and the tunnel, a fully coupled solid-liquid-gas model was developed. This study performed a 2D finite element analysis on the GIL Utility Tunnel. As illustrated in Fig. 1, the whole line of the project was divided into three ranges on the basis of the amount of the shallow gas: the potential distribution area, the distribution area, and the safety area. The major study area was the distribution area; i.e., DK 1 + 0 − DK 1 + 780. The stratigraphic distribution from top to bottom was as follows: No. 3 muddy silty clay, No. 41 silty clay mixed with silty soil, No. 51 silty fine sand, No. 52 fine sand, No. 61 medium-coarse sand, No. 7 silty fine sand, No. 81 medium-coarse sand, and No. 82 silty fine sand. Based on the site drillings, the shallow gas was mainly found in the No. 41, 51, and 52 layers, and the components of these layers were mainly sandy soils, which means that the gas can easily migrate in the soils.

Although the gas reservoirs were widely distributed in the strata where the project was located, it was the gas reservoir with a relatively large volume or the gas reservoir group with connectivity within a certain range that has a significant impact on the project. Existing exploration methods can only obtain the gas reservoir information at the collection point by drilling holes, and the distribution of the gas reservoirs in a larger range and the connectivity between the gas reservoirs cannot be obtained by the existing methods, which also brings great constraints to the fine modeling of the gas-bearing formation. In order to study the long-term impact of the large-scale gas reservoirs on the shield tunnel structure, it is necessary to simplify the geological conditions and establish a geological model which is in line with the actual situation. Figure 2 shows the calculation model. The inner diameter of the tunnel was 10.5 m, the outer diameter was 11.6 m, and the elevation of the tunnel center point was −69 m. The soil system comprised two layers. The upper layer of silty clay behaved as a gas capping layer due to its low permeability. Conversely, the lower layer as a gas reservoir was composed of fine sand with high permeability. The gas reservoir was deposited at the bottom of the capping layer, with a thickness of 14 m and a width of 60–80 m, and the cross-section was trapezoidal as shown in Fig. 2.

3.2 Boundary conditions and initial conditions

According to the hydrogeological survey, it is assumed that the gas only exists in the domain of *DEFG* as shown in Fig. 2. Due to the small gap between the segmental joints, the gas and the water penetrate through the gap under the pressure gradient. The seepage velocity can be calculated by the fracture flow theory (Lomize, 1951; Jiang, 2014):

$$\boldsymbol{n} \cdot \rho_{\text{w}} \overset{\sim}{\boldsymbol{v}}^{\text{ws}} = -\rho_{\text{w}} \frac{\kappa_{\text{c}} k_{\text{crw}}}{\mu_{\text{w}}} \frac{(p_{\text{wb}} - p_{\text{w}})}{L}, \tag{28}$$

$$\boldsymbol{n} \cdot \rho_{\text{g}} \overset{\sim}{\boldsymbol{v}}^{\text{gs}} = -\rho_{\text{g}} \frac{\kappa_{\text{c}} k_{\text{crg}}}{\mu_{\text{g}}} \frac{(p_{\text{gb}} - p_{\text{g}})}{L}, \tag{29}$$

$$\overset{\sim}{\boldsymbol{v}}^{\text{ws}} = -\frac{\boldsymbol{\kappa} k_{\text{rw}}}{\mu_{\text{w}}} (\nabla p_{\text{w}} - \rho_{\text{w}} \boldsymbol{g}), \tag{30}$$

$$\overset{\sim}{\boldsymbol{v}}^{\text{gs}} = -\frac{\boldsymbol{\kappa} k_{\text{rg}}}{\mu_{\text{g}}} (\nabla p_{\text{g}} - \rho_{\text{g}} \boldsymbol{g}), \tag{31}$$

where $\boldsymbol{n}$ is the outward normal unit vector on the boundary; $\overset{\sim}{\boldsymbol{v}}^{\text{ws}}$ and $\overset{\sim}{\boldsymbol{v}}^{\text{gs}}$ are the Darcy seepage velocities of the water and the gas, respectively; κ_{c} is the absolute perme-

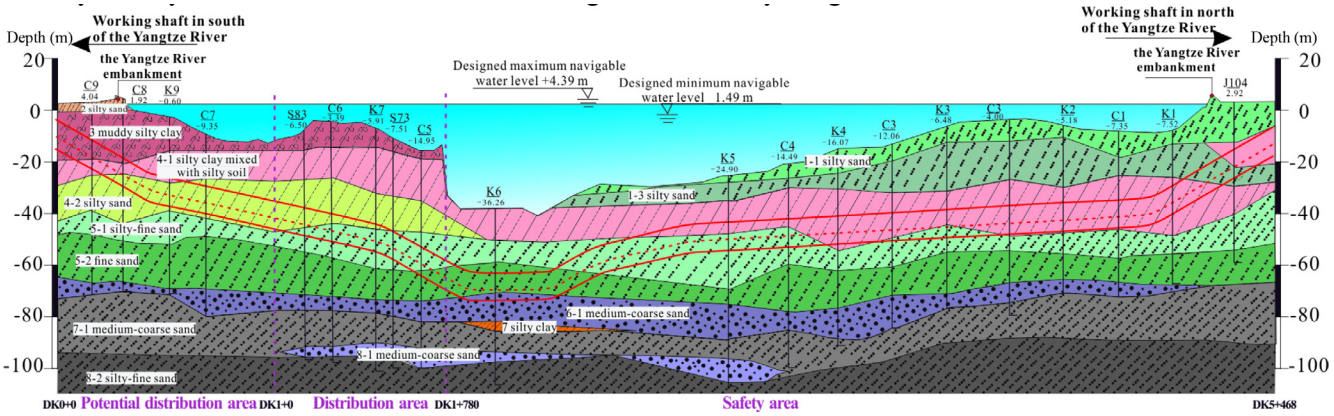

Fig. 1. GIL Utility Tunnel passing through the gas-bearing strata.

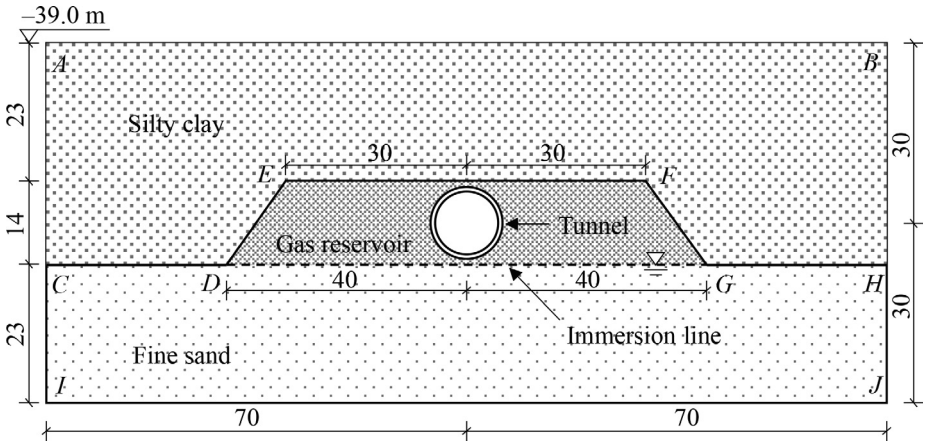

Fig. 2. Calculation model (Unit: m).

ability of the fracture, depending on the geometry of the fracture, such as the width and the roughness; k_{crw} and k_{crg} are the relative permeabilities of the water and the gas, depending on the saturation; p_{wb} and p_{gb} are the external water pressure and the external air pressure (normal atmospheric pressure inside the tunnel); L is the effective crack width (equivalent to per meter along the tunnel).

It should be noted that the boundary *CDEFGH* is the no-flow boundary, the boundary *CIJH* is the constant pressure boundary for the seepage of the pore water, and the boundary *DEFGD* is the no-flow boundary for the seepage of the gas. In the model, the soils above the elevation of −39.0 m were simplified as an applied uniform load. The horizontal displacements of the boundaries AI and BJ were fixed as 0, and all the displacements of the boundary *IJ* were fixed as 0 as well.

According to the geological and hydrological survey, the highest water level of the river is +4.85 m. Hence, the initial pore water pressure distribution is assumed as $p_{w0} = \rho_w g(4.85 - y)$. Since the gas density is much smaller than the water density, the gas pressure is basically constant inside the gas reservoir. Below the immersion line, as shown in Fig. 2, the water phase saturation is 1, the matrix suction is 0, and the gas pressure is equal to the water pressure. Above the immersion line, the gas pressure changes linearly with depth and the initial gas pressure is $p_{g0} = \rho_w g(4.85 + 76) - \rho_g g(y + 76)$.

3.3 Model parameter

The parameters of the soil and the tunnel structure for the multiphase seepage flow are listed in Tables 1–3, respectively. The parameters of the gas were obtained based on the component analysis of the gas collected at the drilling site. The soil parameters came from the geotechnical test report of this project, including the gravity, the porosity, the Poisson's ratio, the residual saturation, and the friction angle. The soil permeability was provided by the on-site and laboratory permeability tests. The slopes of the normal compression curve and the rebound curve were determined according to the curve given by the soil sample compression tests. The slope of the suction-related compression

Table 1
Parameters of the multiphase seepage flow.

Model parameter	Value
Soil water characteristic parameter α (1/Pa)	8.163×10^{-6}
Soil water characteristic parameter m	0.275
Soil water characteristic parameter n	1.5
Soil water characteristic parameter L	0.5
Water density ρ_w (kg/m^3)	1000
Water dynamic viscosity μ_w (Pa · s)	1×10^{-3}
Biogas density ρ_g (kg/m^3)	0.782
Biogas dynamic viscosity μ_g (Pa · s)	1.1697×10^{-5}
κ_c/L (m)	1×10^{-19}

curve and that of the suction-related rebound curve adopted the empirical values of the Shanghai clay (Ye et al., 2005). The material parameters related to the BBMx model (such as the fitting parameters, the tensile strength proportional coefficient, the reference pressure, and the yield surface smoothness parameters) were selected according to the conventional values of similar soils (Ye et al., 2005). The specific physical mechanics and hydraulic paraments, based on the geological survey report of the Sutong Project, are shown in Tables 1–3.

4 Results analysis

4.1 Multiphase seepage flow

(1) Effective saturation

The change of the effective saturation with time is shown in Fig. 3. The effective saturation in the unsaturated area is almost linearly distributed along the y-axis, because the fluid permeability in the soil is much higher than that at the segment joints, so that the gas reservoir is nearly in a hydraulic balanced state, and the saturation is evenly distributed in the horizontal direction. After 10 years, the saturated region gradually expands to the upper part of the strata due to the leakage of the gas through the segment joints until the wetting line reaches the upper edge of the tunnel.

Table 3
Parameters for the tunnel structure.

Model parameter	Value
Elastic Modulus E (MPa)	3×10^4
Poisson's ratio v	0.2
Density (kN/m^3)	25

(2) Fluid pressure and Darcy velocity

Figure 4 shows the pressure and the Darcy velocity of the pore water in the fine sand layer. The pore water pressure distribution is close to hydrostatic and remains almost constant throughout the leakage process. Because of the low seepage velocity of the pore water, it has very limited effects on the distribution of the pore water pressure. On the other hand, the pore water flow moves upward to the tunnel, and the velocity becomes faster near the tunnel due to the water leakage through the segment joints.

(3) Gas and water leakage through the segment joints

The distribution of the gas leakage velocity along the tunnel boundary is shown in Fig. 5(a). The 5 a, 10 a, 15 a, 20 a, 25 a, 30 a, 35 a, and 40 a shown in Fig. 5(a) represent 5 years, 10 years, 15 years, 20 years, 25 years, 30 years, 35 years, and 40 years, respectively. The leakage velocity of the gas is 0 at the position of the immersion line, and increases with elevation until reaching the maximum at the top of the tunnel. This is due to the higher relative permeability coefficient k_{crg} at the top induced by the satura-

Table 2
Soil parameters.

Model parameter	Fine sand	Silty clay
Saturated weight density γ_{sat} (kN/m^3)	20.29	18.49
Dry weight density γ_0 (kN/m^3)	16.41	–
Initial permeability κ_0 (m^2)	4.19×10^{-13}	–
Initial porosity ϕ_0	0.396	–
Water residual saturation S_s	0.07	–
Poisson's ratio μ	0.28	0.35
Compression curve slope in the saturated state λ_0	0.0408	0.1138
Rebound curve slope κ	0.0052 1	0.0126
Suction-dependent compression curve slope λ_s	0.08	–
Suction-dependent rebound curve slope κ_s	0.008	–
Friction angle ϕ (°)	31.3	33.7
Fitting parameter r	0.75	–
Fitting parameter β (Pa)	1.5×10^{-6}	–
Ratio coefficient of tensile strength k_c	1	–
Reference pressure p_{ref} (Pa)	1×10^5	1×10^5
Smoothness parameter of the yield surface B	100	–

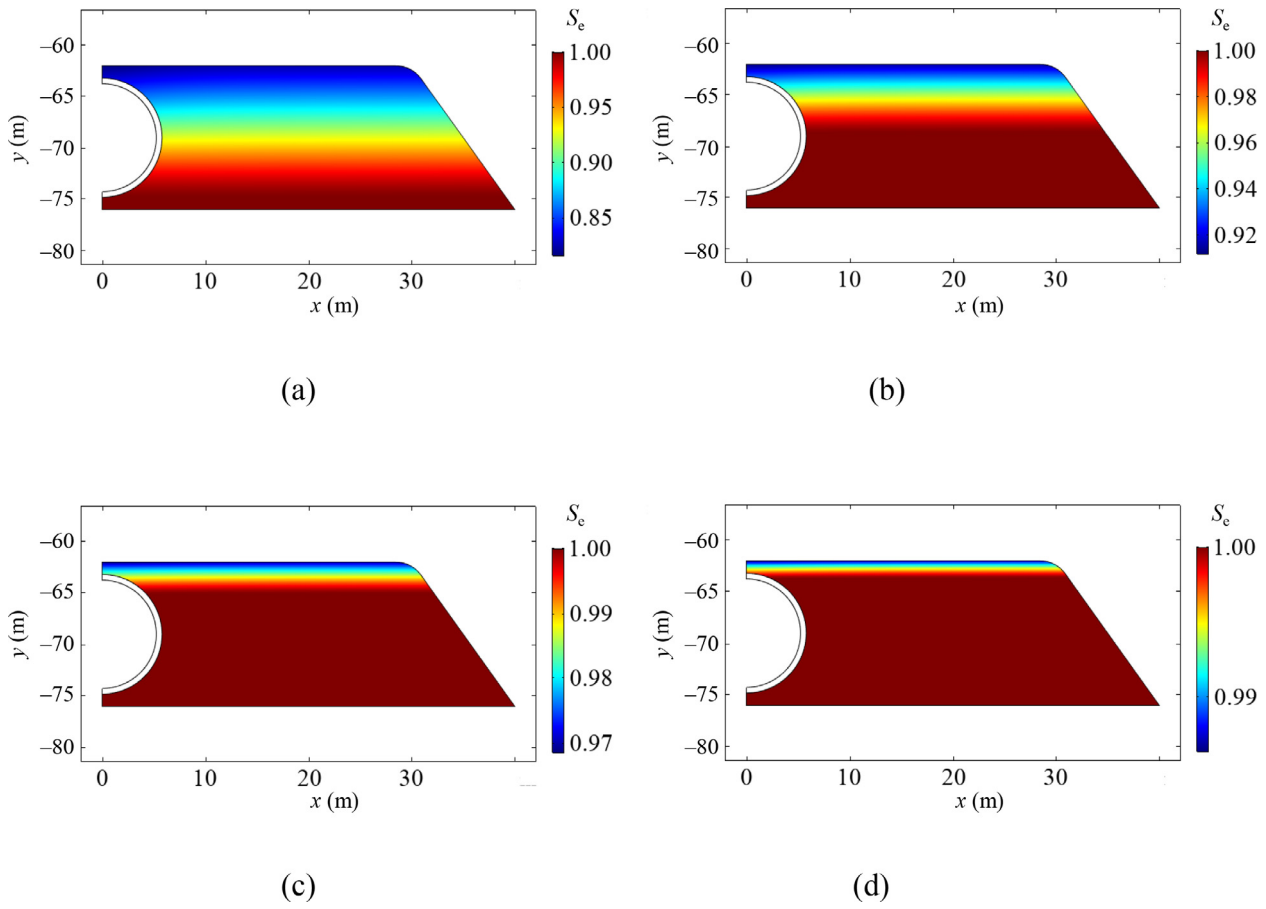

Fig. 3. Gas reservoir effective saturation, S_e after (a) 1 year, (b) 10 years, (c) 20 years, and (d) 30 years.

tion distribution in the gas reservoir. When the tunnel is completely submerged, the gas under the elevation of the tunnel top is exhausted, resulting in a stable residual gas reservoir. Figure 5(b) shows the leakage velocity of the water around the tunnel. Different from the gas, it is shown that the leakage velocity of the lower part is higher than that of the upper part and remains constant with time. This is because the pore water pressure increases with depth, and the change of the pore water pressure during a long period of time is very limited as shown in Fig. 4.

4.2 Soil behavior

(1) Soil displacement and volumetric strain

The displacement of the soil is shown in Fig. 6. Significant upward displacement occurred during the leakage of the gas and the pore water. The displacement in the upper strata is significantly larger than that in the strata below the gas reservoir. There is no obvious displacement away from the gas reservoir. Figure 7 shows the vertical displacements at the feature points over time, in which the deformation of the lower soil reaches the steady state faster than that of the upper soil does. The displacement of the soil increases with time, with the maximum displacement over 30 mm after a period of 30 years, as illustrated in Figs. 6(d) and 7(b). The subsequent uplift amount of point X_1 is 11.04 mm larger than that of point X_5, which shows that the gas-bearing sand has undergone expansion deformation.

The volumetric strain of the soil is mainly controlled by the average effective stress and the matrix suction, as shown in Figs. 8–10. The deformation characteristics of the soil can also be revealed by the volume strain, which is shown in Fig. 8. The gas-bearing strata as well as its underlying layer produces significant dilatant volumetric strain. The strain of the underlying strata is evenly distributed along the vertical direction; however, the strain distribution inside the gas-bearing strata is not uniform, and it develops upward with the same law as the immersion line does, which is shown in Fig. 9. The suction of the soil decreases with time, causing the elastic expansion of the soil skeleton; however, Fig. 10 shows the increment of the average effective stress in the upper part of the gas reservoir, which will cause the compression of the soil. The final volumetric strain of the soil is determined by the combined effects of these two factors; i.e., the average effective stress and the matrix suction. In most areas of the gas reservoir, the hygroscopic expansion exceeds the stress-induced compression; however, in the local area near the top of the tunnel, the effect of compression dominates. In the lower strata, the reduction of the average effective stress results in elastic

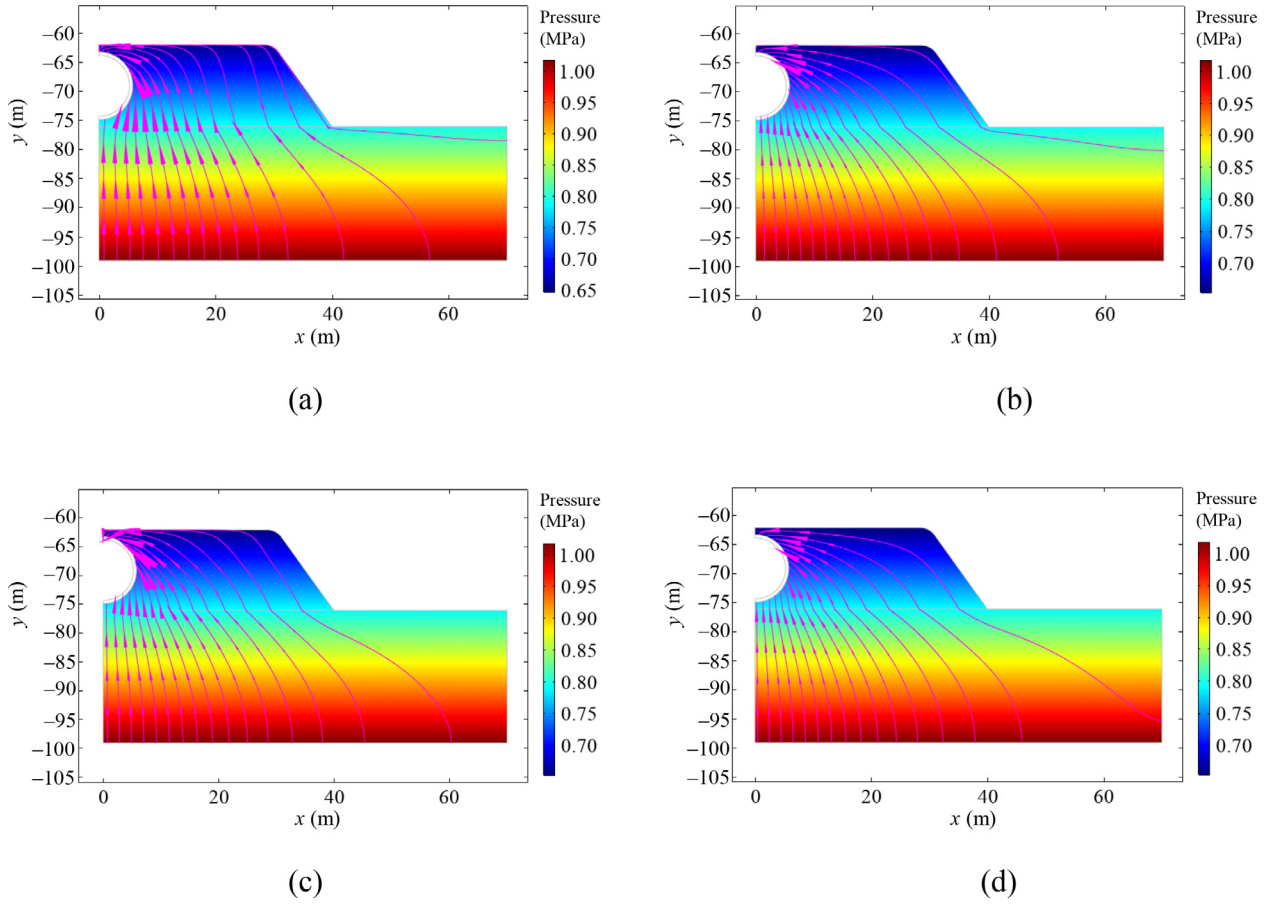

Fig. 4. Pressure and Darcy velocity of the water after (a) 1 year, (b) 10 years, (c) 20 years, and (d) 30 years.

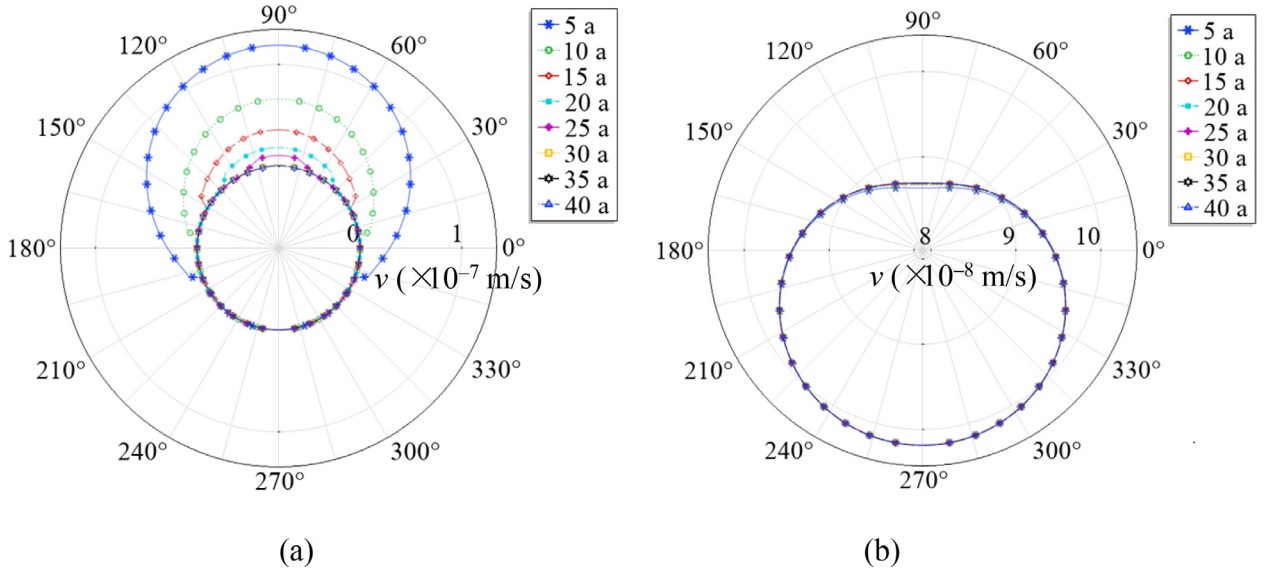

Fig. 5. Leakage velocity and Darcy velocity of the fluids: (a) Gas leakage velocity through the gap, (b) water leakage velocity through the gap.

expansion, whereas the matrix suction remains at 0. In the upper strata, both the average effective stress and the matrix suction remain unchanged, therefore, the soil does not show a significant volumetric strain.

As described above, the increment of the average effective stress is distributed above the soil and below the gas reservoir in the opposite pattern, as shown in Fig. 10. The soil equilibrium equation can be rewritten as

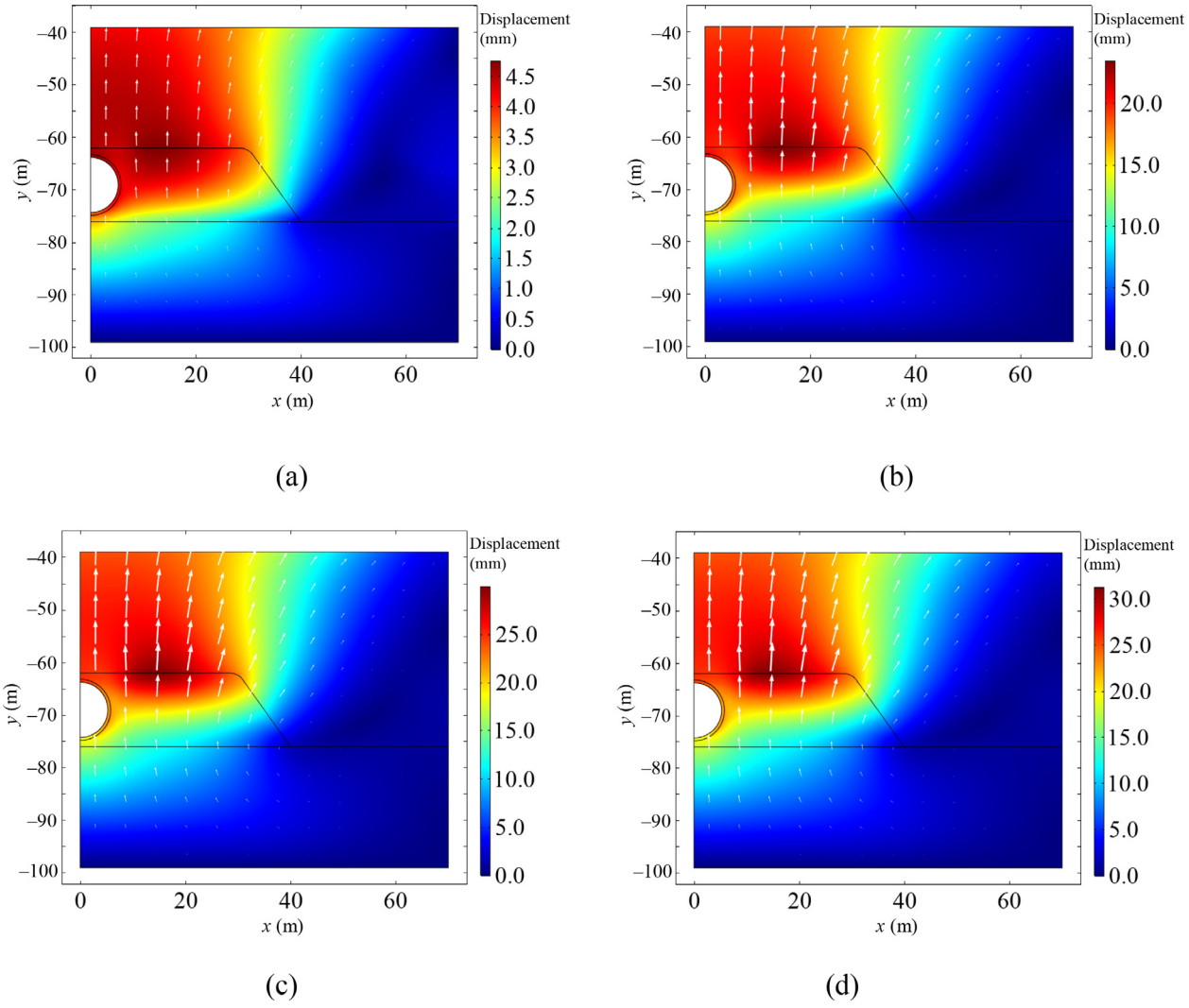

Fig. 6. Soil displacement after (a) 1 year, (b) 10 years, (c) 20 years, and (d) 30 years.

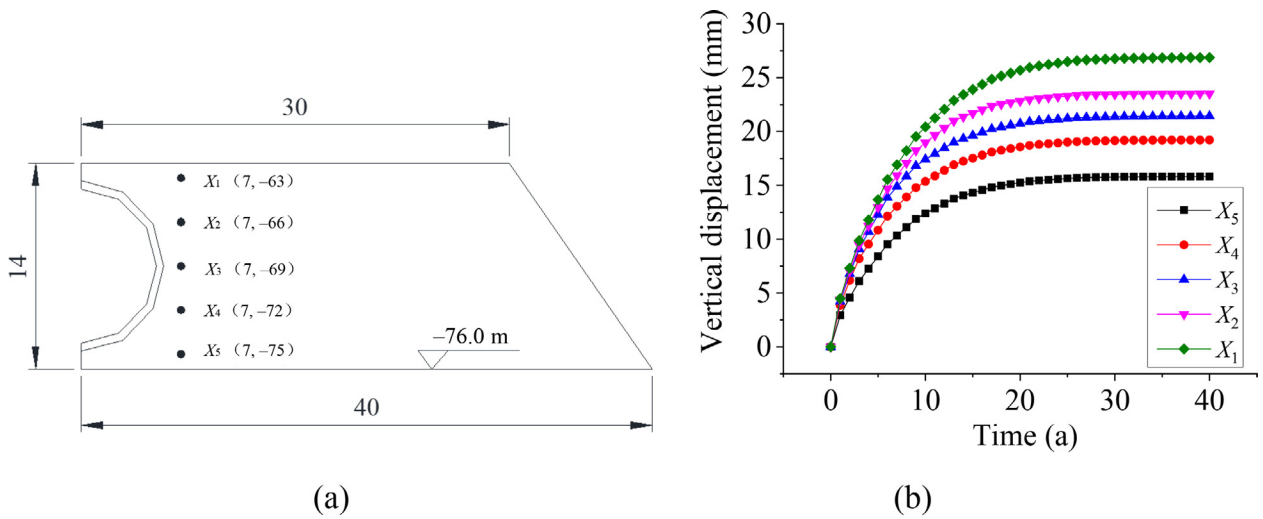

Fig. 7. Vertical displacement of the key points in the gas-bearing reservoir: (a) Feature point coordinates (Unit: m), (b) vertical displacements at the feature points over time (Unit: mm).

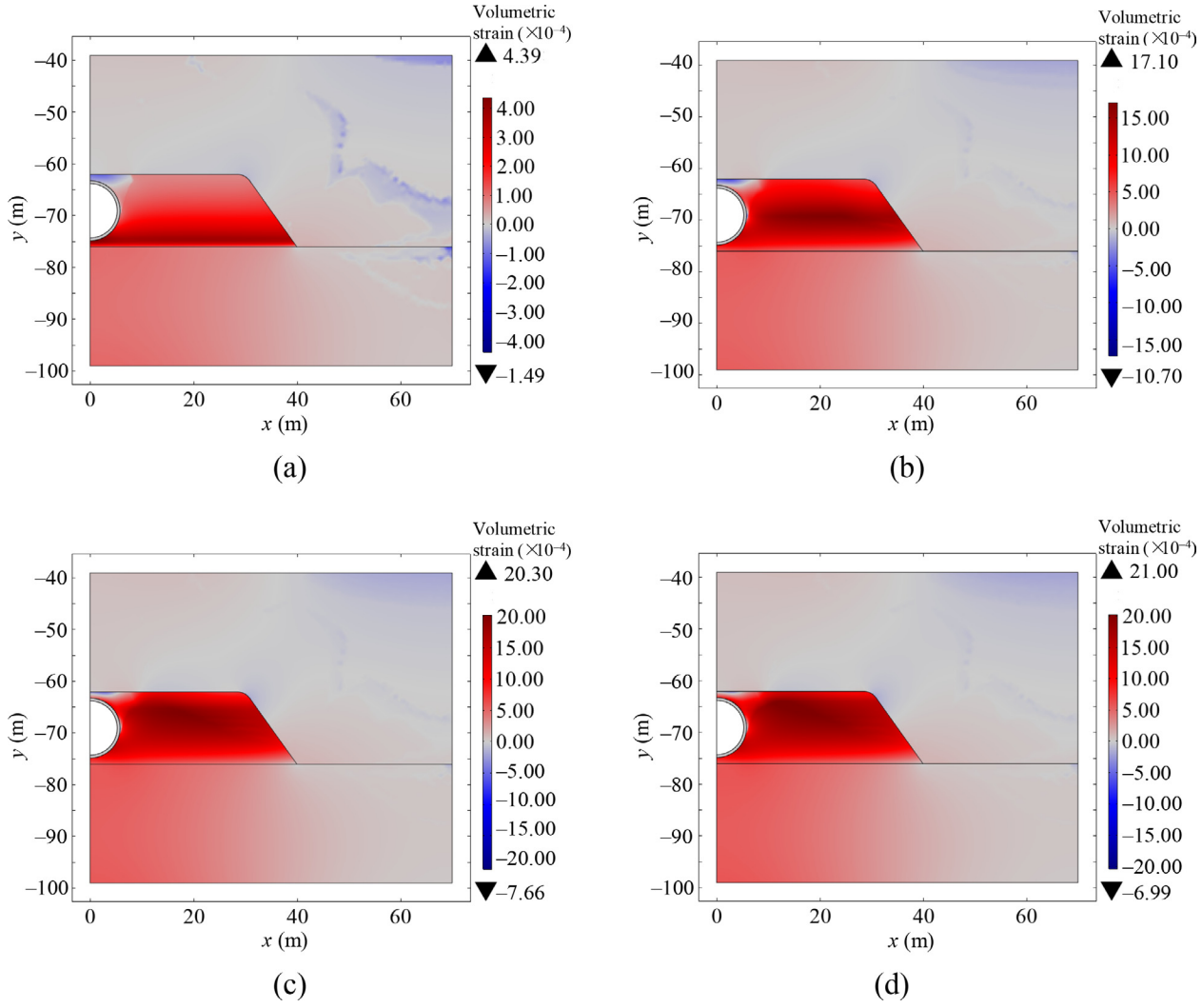

Fig. 8. Volumetric strain after (a) 1 year, (b) 10 years, (c) 20 years, and (d) 30 years.

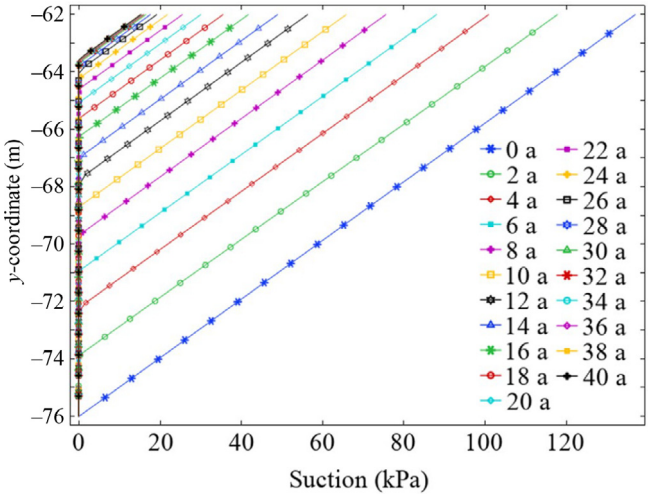

Fig. 9. Matrix suction distribution.

$\nabla \cdot \sigma' + [\gamma_0 + S(\gamma' - \gamma_0)] = 0$, in which $\gamma' = \gamma_{sat} - \gamma_w$. Because of $\gamma' < \gamma_0$, as the saturation increases, the average effective stress of the soil skeleton in the lower strata is reduced. It indicates that the soil in the gas reservoir is subjected to an upward force after the moisture absorption. Therefore, the pressure on the underlying strata is reduced. However, for the soil in the gas reservoir, the change of the total stress is relatively small, and the pore water pressure is significantly reduced due to the gas leakage, which induces an increase in the average effective stress of the soil. In the upper strata, the average effective stress remains unchanged because there's no multiphase seepage flow in this area.

(2) Soil stress

The increment of the Mises stress of the soil after leakage is shown in Fig. 11, which indicates that the shear stresses in the lower strata and the gas-bearing strata are

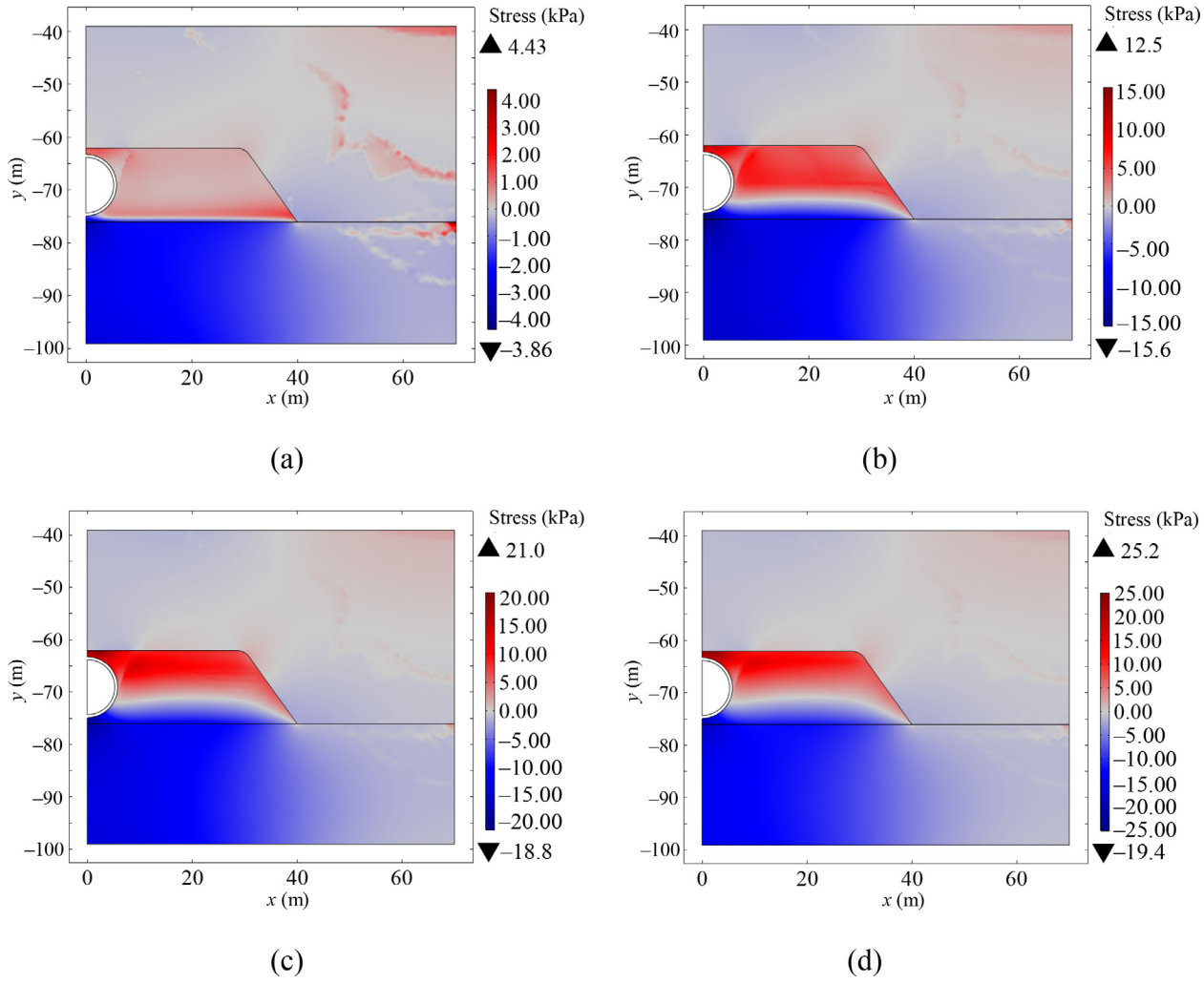

Fig. 10. Increment of the average effective stress after leakage of (a) 1 year, (b) 10 years, (c) 20 years, and (d) 30 years.

significantly reduced. The decrease of σ'_y is greater than that of σ'_x, corresponding to the more strain increment in the y-direction than that in the x-direction. Notice that σ'_y is the maximum principal stress. Therefore, the difference between σ'_y and σ'_x is reduced; i.e., the shear stress is reduced. In the gas-bearing strata, σ'_y decreases due to the increase of the buoyancy. Moreover, a moisture absorption in the layer tends to cause the gas reservoir to be subjected to a horizontal stress from the lateral soil, according to the constitutive model, due to the lateral displacement limitation. Therefore, the increased σ'_x reduces the difference between σ'_y and σ'_x.

Moreover, there exists the moisture absorbing expansion in this layer. The constitutive equation defines an isotropic expansion deformation caused by the moisture absorption, which will cause the gas reservoir to be subjected to a horizontal reaction force from the lateral soil, due to the lateral displacement limitation. As a result, σ'_x increases. However, the expansion deformation does not cause significant reaction force in the y-direction, because σ'_y is mainly determined by the upper soil weight. Finally, the difference between σ'_y and σ'_x is reduced so that the shear stress of the gas-bearing strata is reduced, which is more significant than that of the underlying strata.

The stress paths of the key points in the gas-bearing strata are shown in Fig. 12. The average effective stress of point X_1 increases, while that of point X_5 decreases, and those of points X_2-X_4 increase first and then decrease. The shear stress is reduced for all the points, except for point X_3, which has small fluctuations in the later stage.

The three-dimensional stress path of point X_1 and its yield surface are shown in Fig. 13. An increase in the average effective stress will induce the expansion of the yield surface, and the reduction in the suction will also expand the yield surface. The stress path will cause plastic deformation eventually.

4.3 Tunnel behavior

The variation of the bending moment increments is shown in Fig. 14, where the bending moments are drawn in the polar coordinate system. The top and the bottom

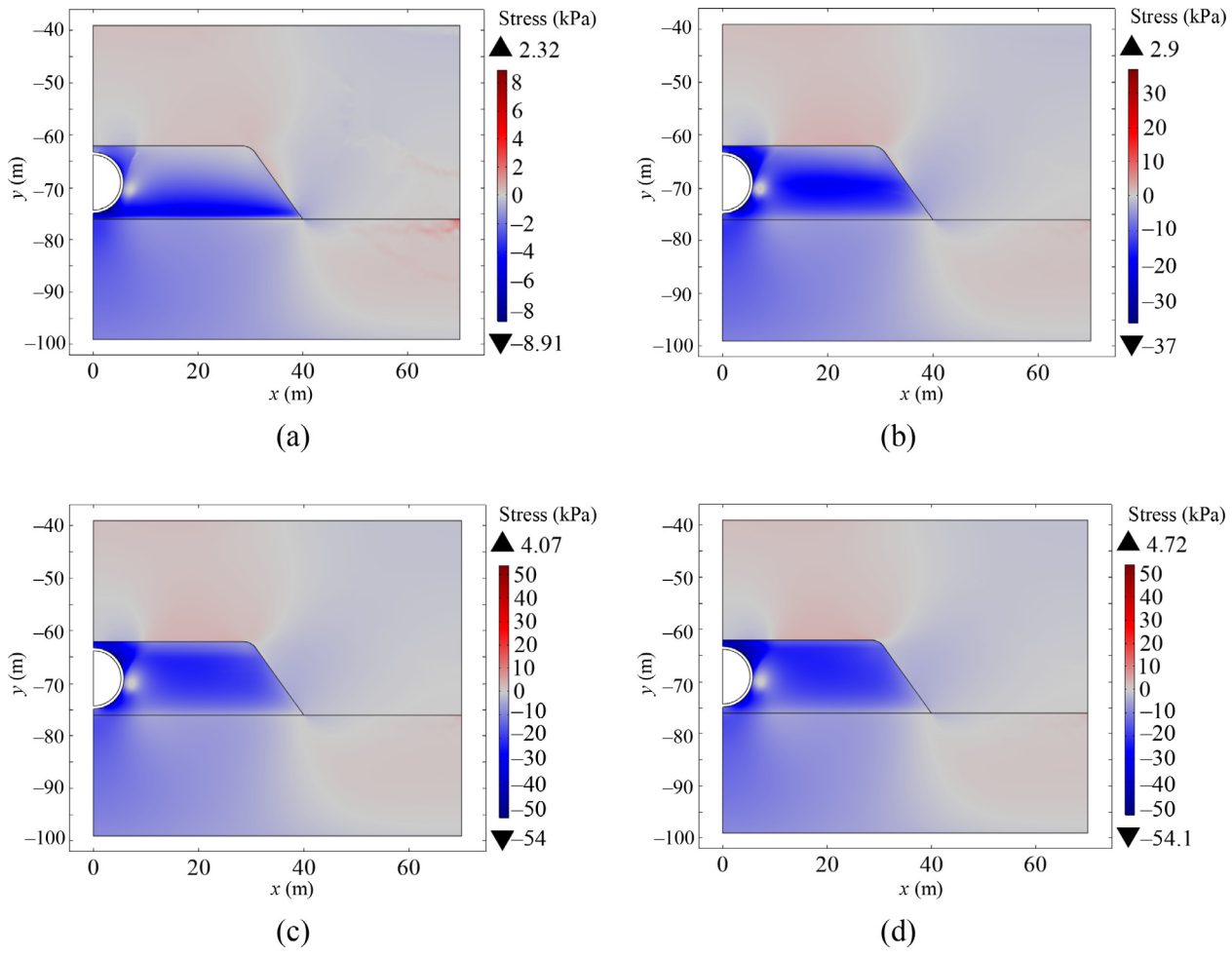

Fig. 11. Mises stress increment after leakage of (a) 1 year, (b) 10 years, (c) 20 years, and (d) 30 years.

of the inner side of the tunnel are in tension at the beginning. After the deformation caused by the leakage is stabilized, the values of the bending moment increments are both about 90 kN · m at the top and the bottom, and −120 kN · m on both the left and right sides of the tunnel. Figure 15 shows the rise of the tunnel's center point and the history of the saturation line position over time. It also indicates that the water level increases over time and reaches a constant level after 30 years. Whereas the tunnel tends to be stable from 20 years onwards. Therefore, soil deformation due to water leakage only occurs at the early stage.

4.4 Performance of the segmental joints

Generally speaking, the bolt arrangement of the segmental joint adopts the "2 + 1" pattern, as shown in Fig. 16(a). However, for the joint between the top sealing block and the adjacent block, in order to avoid the position conflict between the grouting hole and the hand hole on the top sealing block, the three hand holes were all arranged on the adjacent block. (see Fig. 16(b)). Therefore, there were two types of joint forms in the project GIL, as shown in Fig. 16, which are called "bilateral hand hole" and "unilateral hand hole".

Based on the finite element simulation of the solid-liquid-gas coupling problem in the unsaturated soil in the previous section, the internal forces of the tunnel section in the gas-bearing strata were calculated quantitatively. The internal forces under different working conditions were derived, and the extreme values of the positive and the negative bending moments and their corresponding axial forces were extracted as the adverse internal forces combination for the calculation of the joint opening in this section. Four different types of gas reservoir models were considered: down-lying symmetric gas reservoir, a down-lying asymmetric gas reservoir, a middle symmetric gas reservoir, and a middle asymmetric gas reservoir. The segmental joints were not considered in the fully coupled solid-liquid-gas model. The tunnel was regarded as a rigid ring with no reduction in rigidity, which resulted in a larger bending moment for the segmental joints. However, the bending moment at the

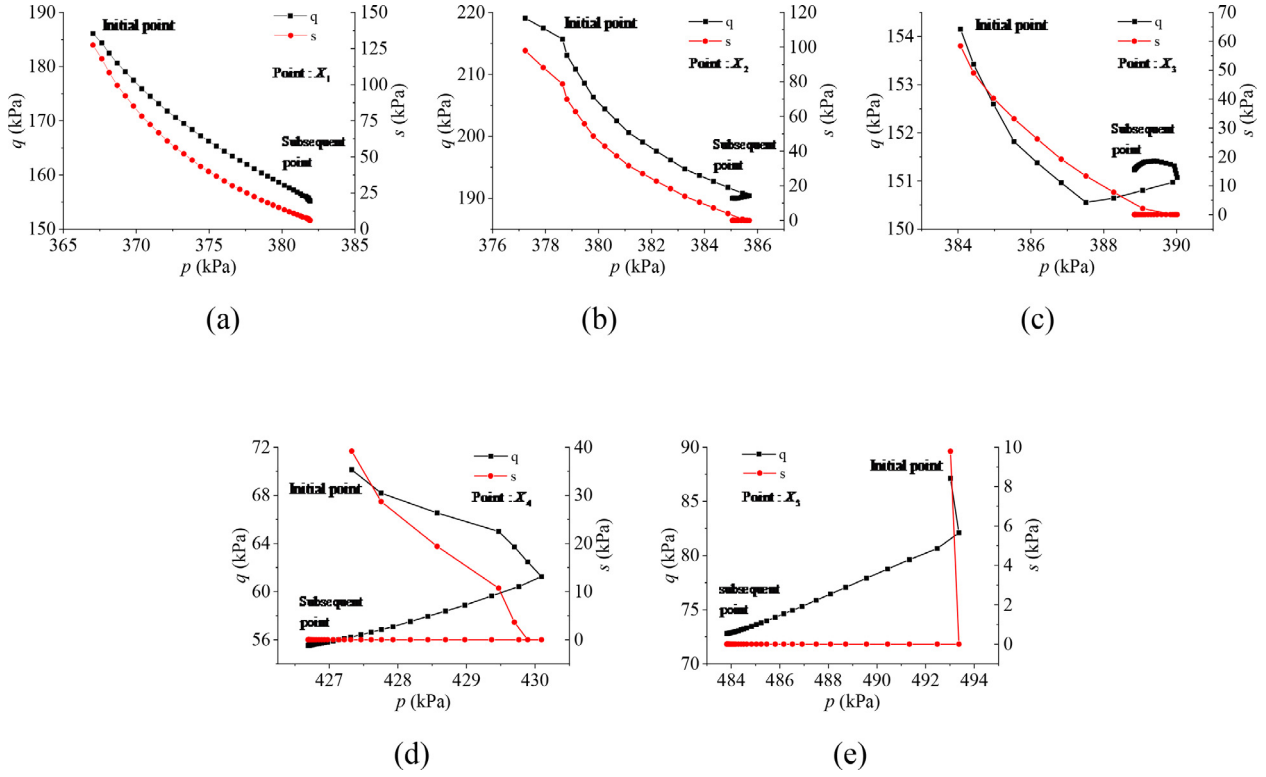

Fig. 12. Soil stress paths of the key points: (a) X_1, (b) X_2, (c) X_3, (d) X_4, and (e) X_5.

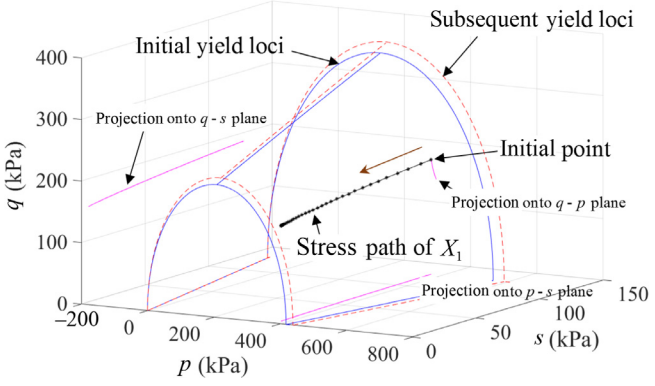

Fig. 13. Stress path of the point X_1 in the three-dimensional space.

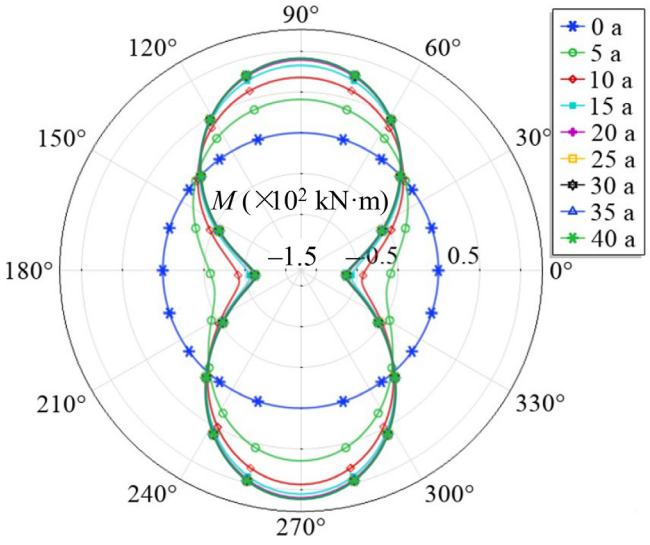

Fig. 14. Bending moment increment.

segmental joints was reduced by a factor of 0.7 before computing its deformation with ABAQUS.

The internal forces of the tunnel linings during the gas leakage were derived, and 4 groups of the unfavourable bending moments and the axial forces were extracted to evaluate the performance of the segmental joints, as shown in Table 4. Accordingly, a 3D finite element analysis was performed to simulate the performance of the segment joints under these combinations of the internal forces, as shown in Fig. 17. In this model, the elastic modulus of the steel bolt was 210 GPa and the yield strength was 900 MPa.

The steel bars and the bolt rods were embedded into the concrete segments. The friction contact with a friction coef-

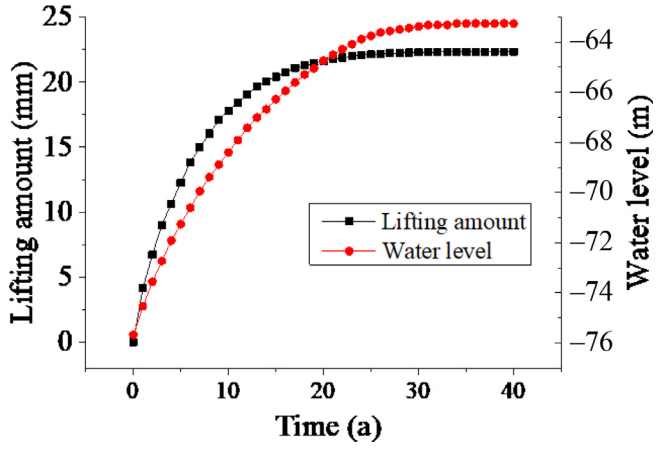

Fig. 15. Lifting amount of the tunnel's center point and the immersion line.

ficient of 0.5 was used to simulate the segment-to-bolt interface and segment-to-segment interface. Because of the water-proof strip at the joints, the contact area was slightly smaller than the cross section of the concrete segments. As shown in Fig. 18, the segment joints were loaded in two cases to simulate the positive and the negative bending moments. By performing a series of analyses, it is found that case 4 would induce the maximum bolt stress of 173 MPa, as shown in Table 5 and Fig. 19. As shown in Fig. 20, the maximum bolt stress obtained by the negative bending moment is 252.3 MPa in case 4. In case 3 with the positive bending moment, the joint opening reaches the maximum value of 0.69 mm, and the corresponding bolt stress is 119.5 MPa, which is much smaller than its yield strength. Therefore, it can be judged that the influence of the high pressure on tunnel safety and the sealing performance of the joints is very limited.

(a) (b)

Fig. 16. Segmental joint prototype: (a) Bilateral hand hole, (b) unilateral hand hole.

Table 4
Unfavorable internal forces combination under different conditions.

Cases	Bending moment symbol	Bending moment (kN · m)	Axial force (kN)
1	Positive moment	1007.44	7079.7
	Negative moment	973.91	8814.9
2	Positive moment	730.17	7308.6
	Negative moment	704.13	8764.3
3	Positive moment	1214.22	6966.4
	Negative moment	1047.48	8897.2
4	Positive moment	879.13	7020.1
	Negative moment	781.13	8941.8

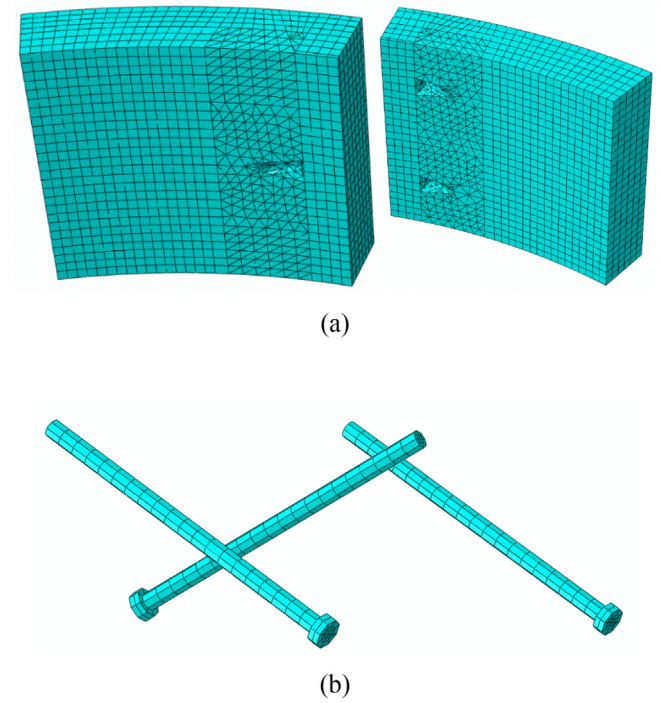

Fig 17. 3D finite element model for the evaluation of the performance of the segment joints: (a) Tunnel segments, (b) steel bolts.

5 Conclusion

This paper develops a fully coupled solid-liquid-gas model to investigate the influence of high-pressure gas on the mechanical properties of the tunnel segments and joints. It also considers the effect of the seepage process on soil deformation utilizing the Extended Barcelona Basic Model (BBMx). The modeling of the BBMx is implemented to simulate the leakage of the gas and the water through the segmental joints. The results are consistent with the basic laws of soil mechanics, which is helpful for the construction and maintenance of shield tunnels.

(1) The results show that the leakage velocity of the gas at the top of the tunnel was greater than that at the bottom, while the leakage velocity of water was the opposite. This is because the gas has a higher volume fraction and permeability at the top of the tunnel, while the pressure of the water increases with depth.
(2) The significant upward displacement occurred in the gas reservoir and its overlying strata. The displacement in the upper strata was greater than that in the strata below the gas reservoir. In addition, the displacement of the soil increased with time, and the maximum displacement was more than 30 mm.

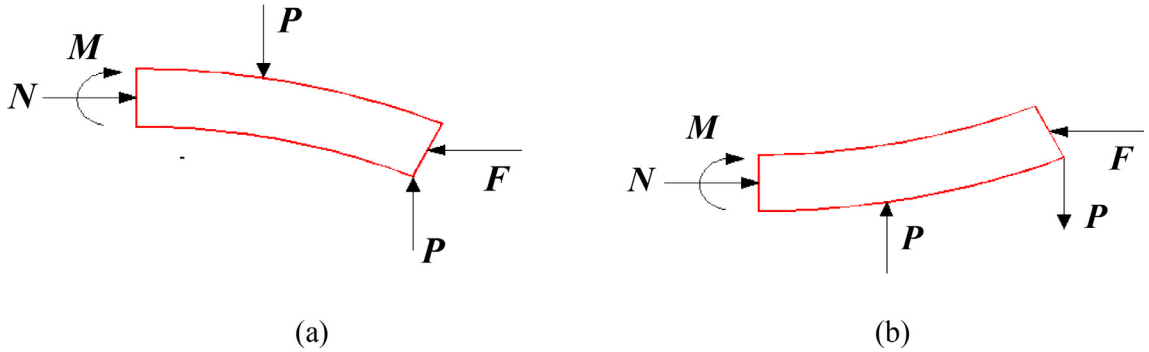

(a) (b)

Fig. 18. Positive and negative bending moment loading modes: (a) Positive bending moment loading, (b) negative bending moment loading.

Table 5
Analysis of results of the joint deformation of the segment under different conditions.

Cases	Loading method	Bending moment (kN · m)	Axial force (kN)	Bolt stress (MPa)	Joint opening (mm)
1	Positive moment	1007.44	7079.7	101.3	0.24
	Negative moment	973.91	8814.9	171.8	0.02
2	Positive moment	730.17	7308.6	84.8	0.02
	Negative moment	704.13	8764.3	172.7	0
3	Positive moment	1214.22	6966.4	119.5	0.69
	Negative moment	1047.48	8897.2	171.8	0.03
4	Positive moment	879.13	7020.1	101.5	0.11
	Negative moment	781.13	8941.8	173	0

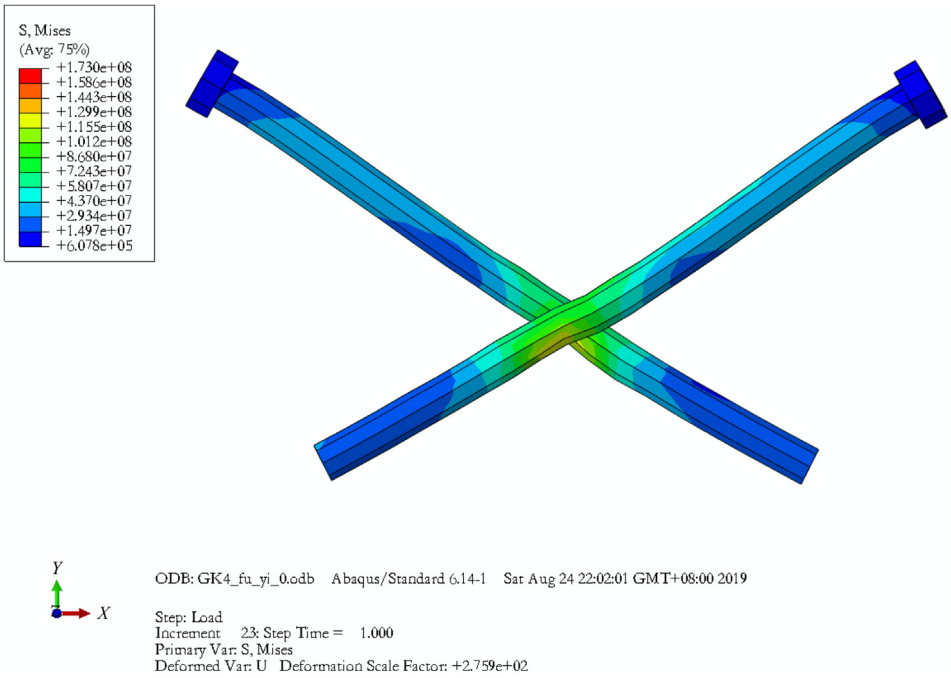

Fig. 19. Distribution of the bolt stress of the bilateral hand hole under the positive bending moments (Unit: Pa).

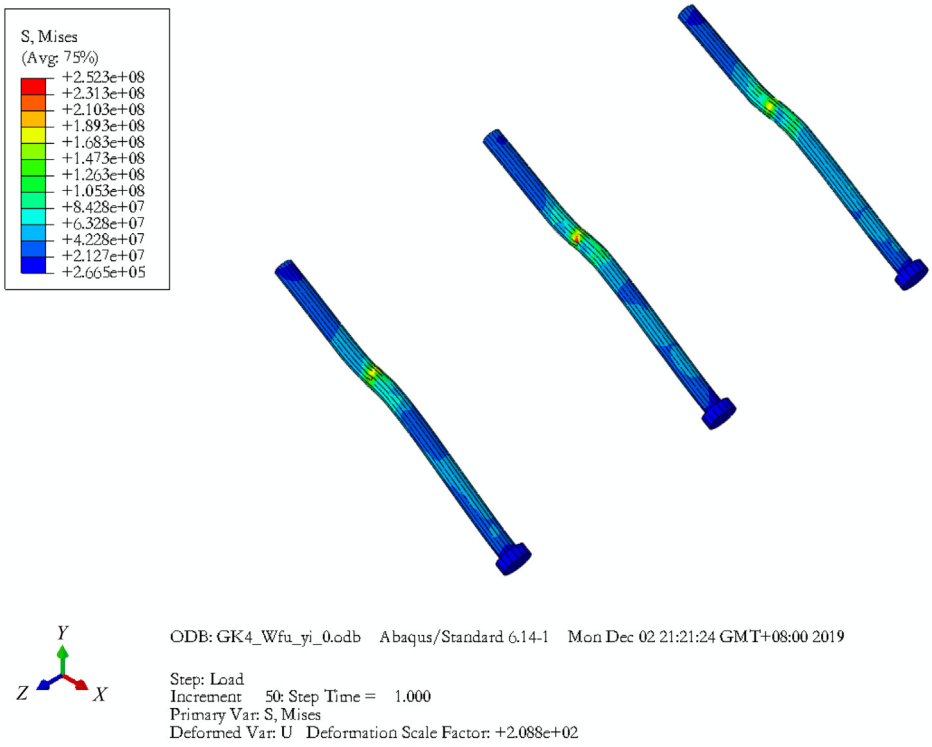

Fig. 20. Distribution of the bolt stress of the unilateral hand hole under the negative bending moments (Unit: Pa).

On the other hand, the volume of the gas-bearing strata increased due to the moisture absorption of the soil.

(3) The plastic deformation of the soil was mainly distributed in the upper part of the gas reservoir, especially on the upper side of the tunnel. An increase

in the average effective stress would induce the expansion of the yield surface, and the reduction in the suction would also expand the yield surface. Eventually, the stress path during the leakage of the gas and the water would cause plastic deformation.

(4) The tunnel tended to be stable from 20 years onwards, so the soil deformation due to the water leakage only occurred at the early stage. After the deformation caused by the leakage was stabilized, the values of the bending moment increments were both about 90 kN · m at the top and the bottom, and −120 kN · m on both the left and right sides of the tunnel.

(5) A 3D finite element analysis was performed to simulate the performance of the segment joints. It is shown that the maximum bolt stress was 173 MPa, which is much smaller than its yield strength. Besides, the maximum opening of the segmental joints reached 0.69 mm. It can be judged that the influence of the high pressure on tunnel safety and the sealing performance of the joints is very limited.

Declaration of Competing Interest

The authors declare that they have no known competing financial interests or personal relationships that could have appeared to influence the work reported in this paper.

Acknowledgment

The research was funded by the fellowship of the National Key R&D Program of China (Grant No. 2018YFB2101000), China Postdoctoral Science Foundation (Grant No. 2019M651580), and The Royal Society International Exchange (IES\R1\211092). All the supports are greatly appreciated.

Appendix I Verification of the fully coupled solid-liquid-gas model

In order to verify the fully coupled solid-liquid-gas model, the Liakopoulos drainage test (Liakopoulos, 1964) was simulated using the methodology proposed in this study. The test apparatus is shown in Fig. A1. The sand column was 1 m in height and 0.1 m in diameter. A permeable stone was arranged at the bottom of the sand column, so that the water can be discharged through the permeable stone. An impermeable rigid cylinder was set on the side to restrict the lateral deformation of the sand column. The test was carried out at room temperature (20 ℃). First, the water was injected at the top of the sand column to make the water flow through the sand column and discharged through the permeable stone, and to ensure that the sand column was completely saturated and the flow field reached a steady state. At the beginning of the test, the water injection was stopped, so that the pore water in the sand column could be discharged freely under gravity. At the same time, some important data were recorded, including the water pressure at each point in the sand column, the drainage speed at the bottom, and the accumulated drainage volume during the test.

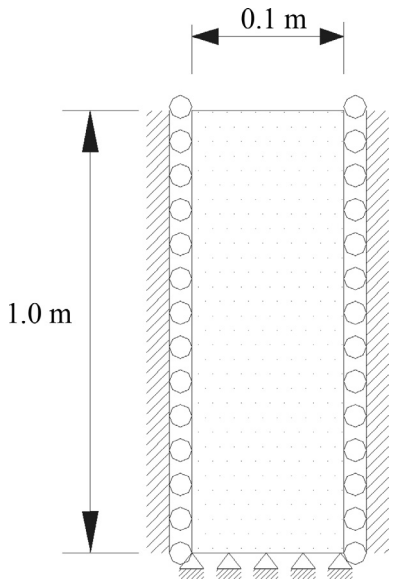

Fig. A1. Test apparatus.

The linear elastic model was used to simulate the sand. When the water flow reached a steady state and the sand was saturated with water, the pore water pressure inside the sand was set as 0 kPa. In addition, the air and water pressures were set as the reference value of 0 kPa. It was assumed that the sand was fully consolidated. For the water seepage field, the upper boundary and side boundary were set as impermeable. The bottom boundary was set as the constant pressure of 0 kPa. For the gas seepage field, the upper boundary and the bottom boundary were constant pressure 0 kPa, and for the side boundary, they were also set as constant pressure. All the parameters used in this model are listed in Table A1.

The drainage rate at the bottom is shown in Fig. A2. It is shown that the numerical simulation results are a little different from the test results at the initial stage of the test, but they are in good agreement at the later stage. Figure A3 shows the change process of the cumulative drainage vol-

Table A1
Model parameter for the Liakopoulos drainage test.

Parameter	Value
Young's Modulus E (MPa)	1.3
Poisson's ratio ν	0.4
Relative permeability of gas k_{rg} (m/s)	1.0×10^{-4}
Particle density ρ_s (kg/m^3)	2850
Initial porosity n_0	0.2975
Water density ρ_w (kg/m^3)	1000
Water dynamic viscosity μ_w (Pa•s)	1.0×10^{-3}
Air density ρ_{a0} (kg/m^3)	1.25
Air dynamic viscosity μ_g (Pa•s)	1.8×10^{-5}

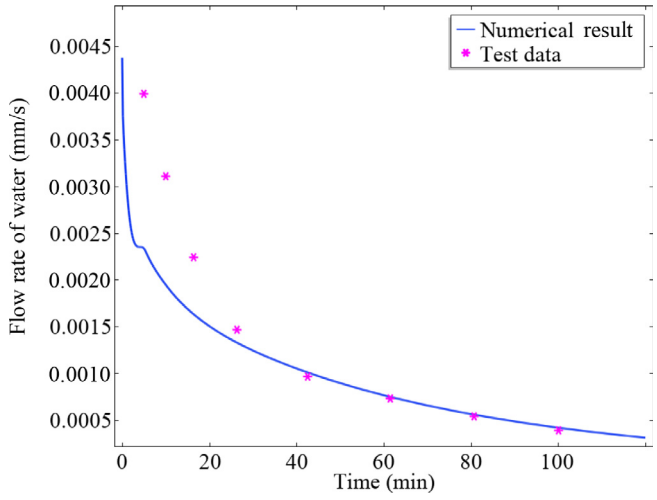

Fig. A2. Drainage rate at the bottom.

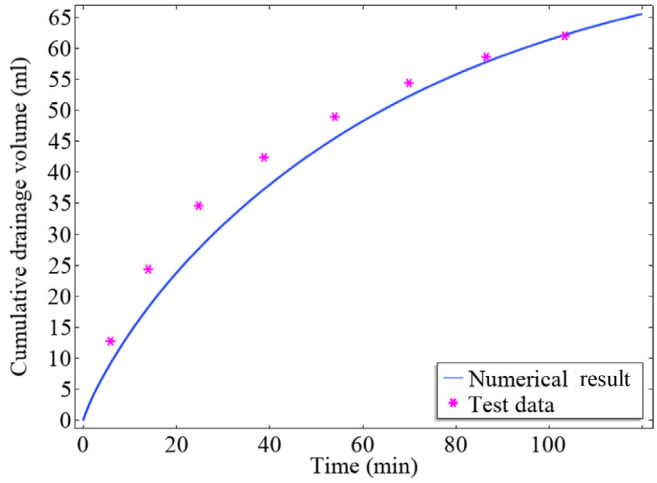

Fig. A3. Cumulative drainage volume.

ume at the bottom. The numerical simulation results are basically consistent with the test data, that is, the cumulative drainage volume gradually increases, and the drainage rate continues to decrease due to the reduction of the relative permeability.

Figure A4 shows the pore pressure distribution along the center line of the sand column. At the beginning of the test, a large negative air pressure occurred at the top of the sand column, and the pressure gradient was large, making the gas infiltration rate relatively high. With the continuous infiltration of the gas, the negative air pressure area gradually shifted to the middle and lower part of the sand column. On the other hand, the negative air pressure and the pressure gradient gradually decreased, which made the gas infiltration rate decrease as well. As the pore water was gradually discharged and tended to be stable, the air infiltration was also gradually weakened, and finally, the pore pressure in the specimen tended to the atmospheric pressure.

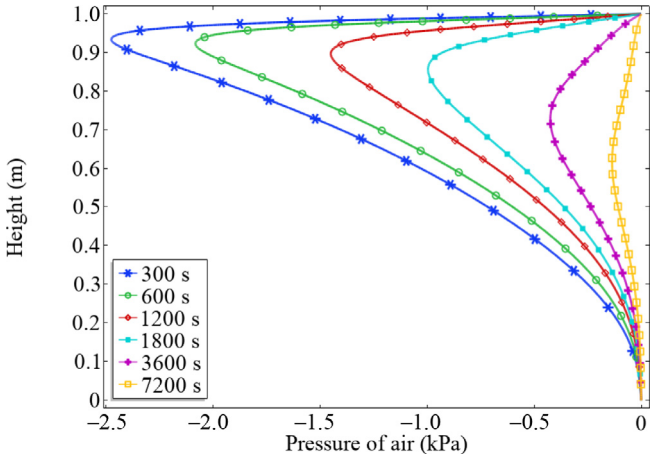

Fig. A4. Air pressure distribution along the center line of the sand column.

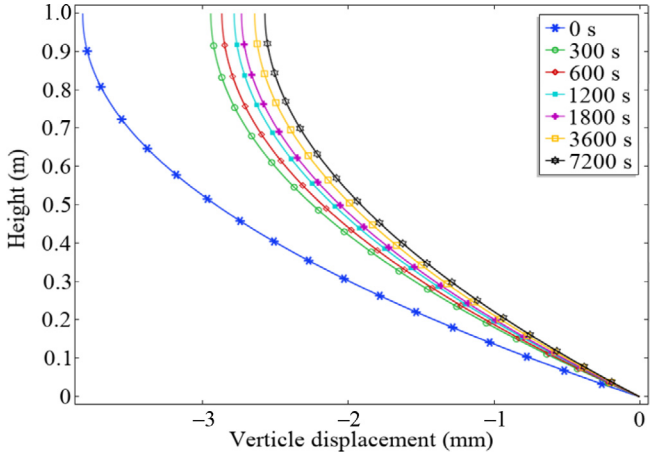

Fig. A5. Vertical displacement of the sand column.

The vertical displacement of the sand column is shown in Fig. A5. It can be seen that the sand column had an initial compressive deformation due to gravity, and the vertical compressive strain of the sand at the lower part was greater than that at the upper part. With the gradual discharge of the pore water, the effective stress on the sand column skeleton gradually decreased, causing the elastic rebound of the sand column.

References

Alonso, E. E., Gens, A., & Josa, A. (1990). A constitutive model for partially saturated soils. *Géotechnique, 40*(3), 405–430.

Biot, M. A. (1941). General theory of three-dimensional consolidation. *Journal of Applied Physics, 12*(2), 155–164.

Bishop, A. W. (1959). The principle of effective stress. *Teknisk ukeblad, 39*, 859–863.

Cai, G. Q., Zhao, C. G., & Tian, H. (2013). Numerical simulation of coupled thermo-hydro-mechanical behavior for engineered barriers in high-level radioactive waste disposal. *Chinese Journal of Geotechnical Engineering, 35*, 1–8 (in Chinese).

Ding, W., Gong, C., Mosalam, K. M., & Soga, K. (2017). Development and application of the integrated sealant test apparatus for sealing

gaskets in tunnel segmental joints. *Tunnelling and Underground Space Technology, 63*, 54–68.
Feng, X., Ye, B., Zhang, X., Dai, Y., & Xia, F. (2021). Analysis of the effects of shallow gas on a shield tunnel during leakage: A case study from the Sutong River-Crossing GIL utility tunnel project in China. *KSCE Journal of Civil Engineering, 25*(6), 2285–2299.
Gong, C., Ding, W., Soga, K., Mosalam, K. M., & Tuo, Y. (2018). Sealant behavior of gasketed segmental joints in shield tunnels: An experimental and numerical study. *Tunnelling and Underground Space Technology, 77*, 127–141.
Guo, A. G., Kong, L. W., Shen, L. C., Zhang, J. R., Wang, Y., Qin, J. S., & Huang, X. F. (2013). Study of disaster countermeasures of shallow gas in metro construction. *Rock and Soil Mechanics, 34*(3), 769–775.
Guo, A., Shen, L., Zhang, J., Qin, J., Huang, X., & Wang, Y. (2010). Influence model analysis of shallow gas on Hangzhou Metro Project construction. *Journal of Railway Engineering Society, 27*(9), 78–81 (in Chinese).
Hu, R. (2013). *A fully coupled hydromechanical model for unsaturated soils and its numerical simulations*. [Doctoral dissertation, Wuhan University, China]. (in Chinese).
Jiang, G. (2014). *Experimental research on gas-water two phase flow characteristics in rock fractures*. [Doctoral dissertation, China University of Mining, China]. (in Chinese).
Liakopoulos, A. C. (1964). *Transient flow through unsaturated porous media*. [Doctoral dissertation, University of California, Berkeley, USA].
Liao, H. J., & Jian, J. I. (2008). Coupled analysis of seepage-settlement for saturated-unsaturated soil in deep foundation pit excavation. *Ying Yong Li Xue Xue Bao/Chinese Journal of Applied Mechanics, 25*(4), 637–640 (in Chinese).
Lomize, G. M. (1951). Flow in fractured rocks. *Gosenergoizdat, Moscow, 127*(197), 635.
Matsuoka, H., & Nakai, T. (1974). Stress-deformation and strength characteristics of soil under three different principal stresses. In *Proceedings of the Japan Society of Civil Engineers* (Vol. 1974, No. 232, pp. 59–70). Japan Society of Civil Engineers.
Nagel, F., & Meschke, G. (2010). An elasto-plastic three phase model for partially saturated soil for the finite element simulation of compressed air support in tunnelling. *International Journal for Numerical and Analytical Methods in Geomechanics, 34*(6), 605–625.
Pedroso, D. M., & Farias, M. M. (2011). Extended Barcelona basic model for unsaturated soils under cyclic loadings. *Computers and Geotechnics, 38*(5), 731–740.
Qi, T. Y., Lei, B., Wang, R., Li, Y., & Li, Z. Y. (2018). Solid-fluid-gas coupling prediction of harmful gas eruption in shield tunneling. *Tunnelling and Underground Space Technology, 71*, 126–137.
Van Genuchten, M. T. (1980). A closed-form equation for predicting the hydraulic conductivity of unsaturated soils. *Soil Science Society of America Journal, 44*(5), 892–898.
Wang, Y., Kong, L., Wang, Y., Wang, M., & Cai, K. (2018). Deformation analysis of shallow gas-bearing ground from controlled gas release in Hangzhou Bay of China. *International Journal of Geomechanics, 18*(1).
Yang, D. (1992). Two-dimensional generalized consolidation nonlinear numerical model of unsaturated soil. *Chinese Journal of Geotechnical Engineering, 14*(S1), 2–12 (in Chinese).
Ye, W. M., Tang, Y. Q., & Cui, Y. J. (2005). Measurement of soil suction in laboratory and soil-water characteristics of Shanghai soft soil. *Chinese Journal of Geotechnical Engineering, 27*(3), 347–349 (in Chinese).
Zhu, Y., Zhou, J., Zhang, B., Wang, H., & Huang, M. (2022). Statistical analysis of major tunnel construction accidents in China from 2010 to 2020. *Tunnelling and Underground Space Technology, 124*, 104460.